Inorganic Chemistry

pubs.acs.org/IC Article

Sites and Mobility of Lithium along the $Li_{1+x}Ti_{2-x}In_x(PO_4)_3$ ($0 \leq x \leq 2$) Series Deduced by XRD, NMR, and Impedance Spectroscopy

Radhouene Kahlaoui,* Kamel Arbi, Isabel Sobrados, Ricardo Jimenez, Riadh Ternane, and Jesus Sanz

Cite This: *Inorg. Chem.* 2024, 63, 7806−7819 Read Online

ACCESS | Metrics & More | Article Recommendations | Supporting Information

ABSTRACT: The structure and Li conductivity has been investigated in the $Li_{1+x}Ti_{2-x}In_x(PO_4)_3$ ($0 \leq x \leq 2$) series prepared by the ceramic route at 900 °C. The XRD patterns of $0 \leq x \leq 0.2$ samples show the presence of rhombohedral (S.G. $R\bar{3}c$); those of $0.2 \leq x \leq 1$ samples display both rhombohedral and orthorhombic (S.G. *Pbca*), and $1 \leq x \leq 2$ samples exhibit only monoclinic (S.G. $P2_1/n$) phases. At intermediate compositions, the secondary $LiTiPO_5$ phase was detected. The Rietveld analysis of XRD patterns was used to deduce unit-cell parameters, chemical composition, and percentage of phases. The amount of In^{3+}, deduced from structural refinements of three phases, was confirmed by ^{31}P MAS NMR spectroscopy. The Li mobility was investigated by ^{7}Li MAS NMR and impedance spectroscopies. The Li conductivity increased with the Li content in rhombohedral but decreased in orthorhombic, increasing again in monoclinic samples. The maximum conductivity was obtained in the rhombohedral $x = 0.2$ sample ($\sigma_b = 1.9 \times 10^{-3}$ S·cm^{-1}), with an activation energy $E_b = 0.27$ eV. In this composition, the overall Li conductivity was $\sigma_{ov} = 1.7 \times 10^{-4}$ S·cm^{-1} and $E_{ov} = 0.32$ eV, making this composition a potential solid electrolyte for all-solid-state batteries. Another maximum conductivity was detected in the monoclinic $x \sim 1.25$ sample ($\sigma_{ov} = 1.4 \times 10^{-5}$ S·cm^{-1}), with an activation energy $E_{ov} = 0.39$ eV. Structural models deduced with the Rietveld technique were used to analyze the conduction channels and justify the transport properties of different $Li_{1+x}Ti_{2-x}In_x(PO_4)_3$ phases.

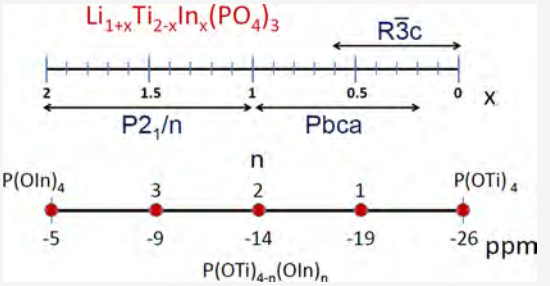

1. INTRODUCTION

Lithium-ion batteries (LIBs) have undergone continuous improvements in lifetime, safety, cost, efficiency, and reliability since their market launch over 30 years back, after their first commercialization by Sony corporation.[1,2] Despite their commercial success in numerous applications, especially in portable electronic devices, LIBs display limited safety characteristics which makes it undeployable in large-scale electrical energy-storage (EES) applications.[3−5] Therefore, safety accidents widely appear in traditional batteries caused by flammable organic liquid electrolytes.[6,7] Over the past decade years, researchers have devoted massive efforts for developing new battery systems with solid-state electrolytes of high conductivity. Hence, ceramic solid electrolytes are largely studied and proposed for next-generation batteries because of their high durability against temperature and good electrochemical and thermal stabilities against Li metal anodes.[8]

The rhombohedral structure of Na super ionic conductors (NaSICON) $LiM_2(PO_4)_3$ phases (S.G. $R\bar{3}c$) can be described by three-dimensional networks, where PO_4 tetrahedra share oxygens with four MO_6, and MO_6 octahedra share oxygens with six tetrahedra.[10−18] In this structure, two octahedra and three tetrahedra form structural $M_2(PO_4)_3$ units denoted as "lantern units" (Figure 1a). In the conduction channels of NaSICON compounds, Li sites can occupy 6b Wyckoff (M1 sites) coordinated to six oxygens in trigonal antiprisms and 18e Wyckoff (M2 sites) coordinated to eight oxygens.[10−13] In some cases, Li ions can partially occupy midway M1/2 positions between M1 and M2 sites (36f Wyckoff sites).

Since the discovery of NaSICON-type phosphates by Goodenough et al.,[9] researchers have addressed experimental and computational efforts to improve the ionic conductivity and stability of prototype devices. The NaSICON materials are described with the formula, $AM_2(PO_4)_3$, where A denotes alkali (Li^+ and Na^+) cations, and tetravalent M cations (Ge, Ti, Zr, Sn, or Hf) can be substituted by trivalent or pentavalent cations.[9−24] NaSICON materials can display $R\bar{3}c$, $R\bar{3}$, *Ia3d*, *Pbca*, $P2_13$, and $P2_1/n$ symmetry depending on the lattice distortions.[10]

The NaSICON characteristics largely rely on the chemical composition, crystal structure, and unit-cell parameters. These factors are affected by the charge and radii of octahedral and tetrahedral cations. The $LiM_2(PO_4)_3$ phases have been the subject of extensive studies. In M = Zr^{4+}, Sn^{4+}, and Hf^{4+} phases,

Received: January 22, 2024
Revised: March 22, 2024
Accepted: April 4, 2024
Published: April 15, 2024

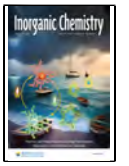

https://doi.org/10.1021/acs.inorgchem.4c00289
Inorg. Chem. 2024, 63, 7806−7819

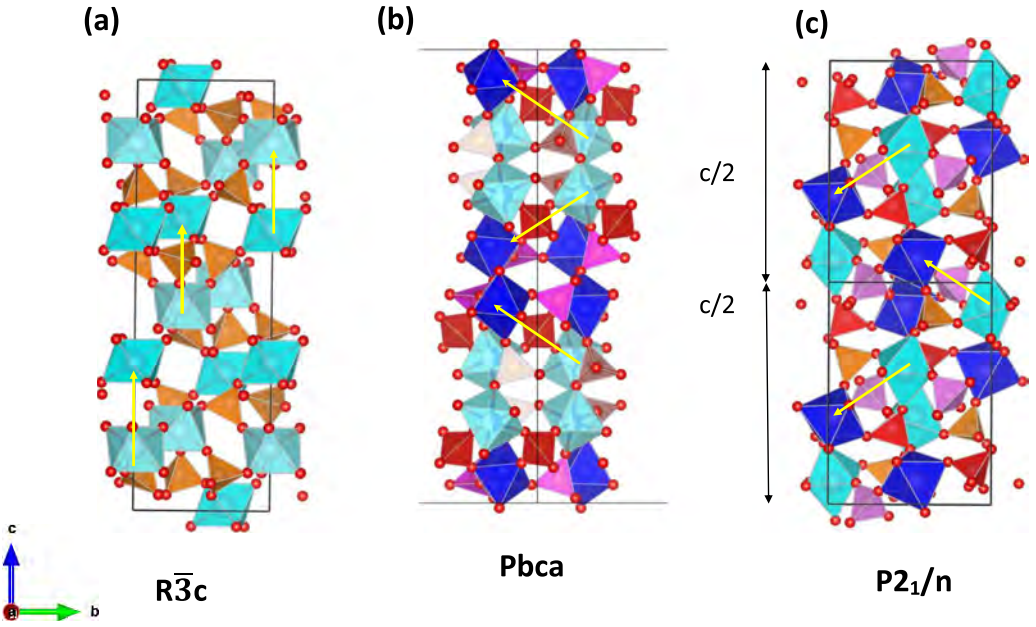

Figure 1. Schematic representation along the [100] direction of (a) rhombohedral, (b) orthorhombic, and (c) monoclinic phases, where orientation of contiguous lanterns is indicated (yellow arrows). In monoclinic phases, the c parameter is half of that of other phases.

a triclinic distortion (S.G. $C\bar{1}$) was reported for low temperatures, which disappears as the temperature increases, giving the rhombohedra symmetry (S.G. $R\bar{3}c$).[21−23] In M = Ti^{4+}, Ge^{4+} phases, the structure only displays the rhombohedral symmetry (S.G. $R\bar{3}c$) in a large temperature interval.[10−16,24] Among NaSICON solid electrolytes, the lithium titanium phosphate $LiTi_2(PO_4)_3$ (LTP) has attracted increasing interest because of its stability, low cost, raw, inherent safety and easy preparation.

In general, the conductivity of solid electrolytes should surpass 10^{-3} S·cm^{-1} for its application in solid-state batteries. Despite the rather promising electrochemical window [ca. −0.52/−0.36 V vs standard hydrogen electrode (SHE)], the $LiTi_2(PO_4)_3$ phase displays a lower Li conductivity ($\sigma \approx 10^{-6}$ S·cm^{-1} at 300 K) than organic electrolytes.[12,13] However, composition is not the sole determinant factor when striving to create an effective solid electrolyte. The synthesis process and the sintering method can be also a powerful strategy to reducing porosity, controlling the microstructure of samples, and improving the electrical performance.

The substitution of tetravalent Ti^{4+} by trivalent cations as Al^{3+}, Sc^{3+}, Fe^{3+}, Y^{3+}, Cr^{3+}, and In^{3+} increases the Li content in Ti NaSICON derivatives.[11−18] In these phases, Li ions occupy, besides M1 sites, M3 sites located near triangular M1/2 windows, increasing considerably Li mobility. The highest conductivity, $\sigma_{bulk} > 10^{-3}$ S·cm^{-1}, was reported in $Li_{1+x}Ti_{2-x}M_x(PO_4)_3$ ($M^{3+} = Al^{3+}$, Sc^{3+}, or In^{3+}) phases with an activation energy of ∼0.25 eV,[13−15] achieving the best results in the $M^{3+} = Al^{3+}$ series. The incorporation of indium (0.80 Å) also enhanced the ionic conductivity of $LiTi_2(PO_4)_3$; however, the structure and ion conduction mechanisms are not well understood.[25] Hamdoune et al.[26] showed the existence of three different $Li_{1+x}Ti_{2-x}In_x(PO_4)_3$ phases: in phase I ($0 \le x \le 0.4$), X-ray diffraction (XRD) patterns display a rhombohedral $R\bar{3}c$ symmetry, in phase II ($0.4 \le x \le 0.1$), orthorhombic *Pbca* symmetry, and in phase III ($1 \le x \le 2$), $P2_1/n$ symmetry. The compositional dependence of the $Li_{1+x}Ti_{2-x}In_x(PO_4)_3$ ($0 < x < 2$) conductivity, measured at 300 °C, revealed two conductivity maxima, the first reaching 2×10^{-2} (Ω·cm)$^{-1}$ at $x \sim 0.35$ and the second 8×10^{-3} (Ω·cm)$^{-1}$ at $x \sim 1.8$.[26] In another work, Qui et al. studied the crystal structure of three $Li_{1+x}Ti_{2-x}In_x(PO_4)_3$ phases by neutron diffraction, showing that the substitution of In^{3+} ions for Ti^{4+} ions produces a rearrangement of Li ions that enhances Li conductivity in rhombohedral phases.[27] In orthorhombic and monoclinic phases, a concerted rotation of structural units produced a zigzag disposition of "lanterns" that affects the disposition of conduction channels (Figure 1b,c).[27]

In this work, the substitution of tetravalent Ti^{4+} by trivalent In^{3+} has been analyzed in $Li_{1+x}Ti_{2-x}In_x(PO_4)_3$ ($0 \le x \le 2$) samples, increasing the charge carrier concentration and improving the Li^+ conductivity. In these samples, the presence of rhombohedral, orthorhombic, and monoclinic phases will be investigated with XRD, NMR, and IS techniques. The use of three techniques affords a better understanding of structure and lithium mobility, which will permit to deduce structural factors that enhances Li conductivity.

2. EXPERIMENTAL SECTION

2.1. Preparation of the Samples. $Li_{1+x}Ti_{2-x}In_x(PO_4)_3$ ($0 \le x \le 2$) compounds were prepared by conventional solid-state reaction. Stoichiometric amounts of $(NH_4)_2HPO_4$ (Roth, >97% purity), TiO_2 (Aldrich, 98% purity), Li_2CO_3 (Merck, >99% purity), and In_2O_3 (Aldrich, 99.9% purity) were carefully mixed using an agate mortar, compressed to form cylindrical pellets, and heated at 180, 300, and 500 °C for 12 h to release water (H_2O), ammonia (NH_3), and carbon dioxide (CO_2). Then, the powders were compressed into cylindrical pellets and heated in air at 700, 800, and 900 °C for 12 h at each temperature with a ramp of 1 °C·min^{-1}. The grinding of pellets after each thermal treatment ensured the samples' homogeneity. To increase the connection between particles and reduce the formation of secondary phases, the grounded pellets were compressed before thermal treatments were performed in Pt crucibles inside a tubular furnace. To analyze the effect of the synthesis temperature on solid solutions, some samples (x = 0.3, 0.4, and 0.5) were also heated at 950 °C.

2.2. Characterization of the Materials. Powder XRD patterns were recorded at room temperature on a Bruker D8-Advance

https://doi.org/10.1021/acs.inorgchem.4c00289
Inorg. Chem. 2024, 63, 7806−7819

diffractometer with a Bragg−Brentano $\theta-2\theta$ geometry with 1.5406 Å Cu-$K_{\alpha 1}$ radiation (40 kV and 30 mA). Measurements were carried out in the 10−90° 2θ range, using a 0.02° step size and a 0.5 s counting/step. The formed phases were identified by comparing their diffraction patterns with those reported by the International Centre for Diffraction Data (ICDD). In Le Bail refinements, the zero pattern, the shape, the full width at half-maximum (fwhm) of peaks, and the unit-cell parameters of phases were determined. Then, structural refinements (atom positions, thermal factors and sites occupancy) were deduced with the Rietveld technique using the Fullprof program.[28,29]

^{6}Li/^{7}Li and ^{31}P NMR spectra were recorded at room temperature in a 9.4T AVANCE-400 Bruker spectrometer at 58.88/155.50 and 161.97 MHz resonance frequencies. In magic-angle spinning (MAS) experiments, the samples were rotated at 10 kHz spinning rates around an axis inclined at 54°44′ with respect to the external magnetic field in 4 mm rotors. For NMR experiments, $\pi/2$ pulse lengths of 4 μs were used for ^{6}Li/^{7}Li and ^{31}P signals and 5, 10, and 180 s intervals were used between successive accumulations. In all cases, the number of scans was in the range 8−400. Aqueous LiCl (1M) and H_3PO_4 (85 wt %) solutions were used as external references for ^{6}Li/^{7}Li and ^{31}P chemical shifts. NMR parameters such us the position, line-width, and intensity of components were fitted by using the standard nonlinear least-squares method implemented in the Winfit Bruker software.[30] Quadrupolar and chemical shift anisotropies of NMR signals were deduced by trial and error procedures.

The morphology of samples was examined by scanning electron microscopy (SEM, JEOL-6010 electron microscope) operating at 20 kV. Samples were deposited on a metallic support and coated with an Au film to eliminate the charge effects. SEM micrographs of the sample were analyzed using ImageJ software. The distributions of Ti, In, and P were investigated with energy-dispersive X-ray spectroscopy in sintered pellets.

The Archimedes method was used to determine the density of $Li_{1+x}Ti_{2-x}In_x(PO_4)_3 (0 \le x \le 2)$ ceramic samples. The relative density of $Li_{1+x}Ti_{2-x}In_x(PO_4)_3$ pellets was determined by computing the ratio between theoretical and measured densities.

In electrical characterization of samples, cylindrical pellets (6 mm diameter and ∼1.8 mm thickness), obtained by applying an uniaxial pressure of 120 MPa, were sintered at 950 °C for 12 h. After sintering, the pellets were polished and the opposite faces were coated with sputtered gold to assess the Li-ion blocking. Impedance spectra (IS) of samples were recorded under vacuum with a 4L-configuration between 243 and 393 K (10 K intervals) in a JANIS VPF 750 cryostat. Measurements were performed in the frequency range of 20 Hz to 2 MHz in an automatically controlled Agilent Precision LCR E4980-A analyzer by applying ac voltage signals of 10 mV. An Agilent E4991-A RF impedance analyzer (operating between 1 MHz and 3 GHz) was used at room temperature to extend the frequency range. The sample was placed at the device port between the inner connector and a short-circuit cap. The fitting of impedance data was performed with Zview software.[31]

3. RESULTS

3.1. Structural Study. To deduce the structure of samples, XRD patterns of $Li_{1+x}Ti_{2-x}In_x(PO_4)_3$ $(0 \le x \le 2)$ samples were collected in the 10−90° angular interval (Figure 2) and compared with the diffraction patterns reported by the International Centre for Diffraction Data (ICDD). The unit-cell parameters were deduced with the Le Bail technique. The XRD patterns of $0 \le x \le 0.1$ samples were fitted with the rhombohedral $R\bar{3}c$ model (JCDPS no. 035-0754). However, the XRD pattern of $0.2 \le x \le 0.75$ required the consideration of orthorhombic *Pbca* (JCDPS no. 040-0029) and rhombohedral $R\bar{3}c$ phases (Figure 2). Finally, the XRD patterns of $1 \le x \le 2$ samples were reproduced with the monoclinic $P2_1/n$ model (JCDPS no. 049-1183). Structural models used in refinements are given as Supporting Information (Tables S1−S3). At intermediate compositions (x = 0.5), the $LiTiPO_5$ phase was included as the secondary phase. The result of this analysis is given in Table S4.

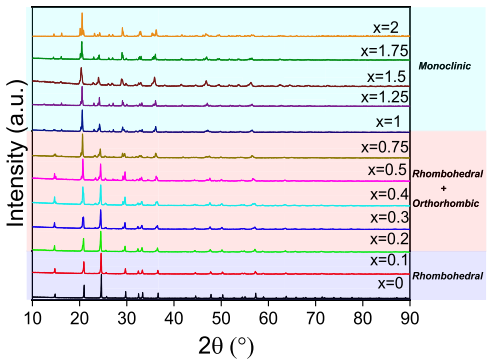

Figure 2. Powder XRD patterns of $Li_{1+x}Ti_{2-x}In_x(PO_4)_3$ $(0 \le x \le 2)$ samples.

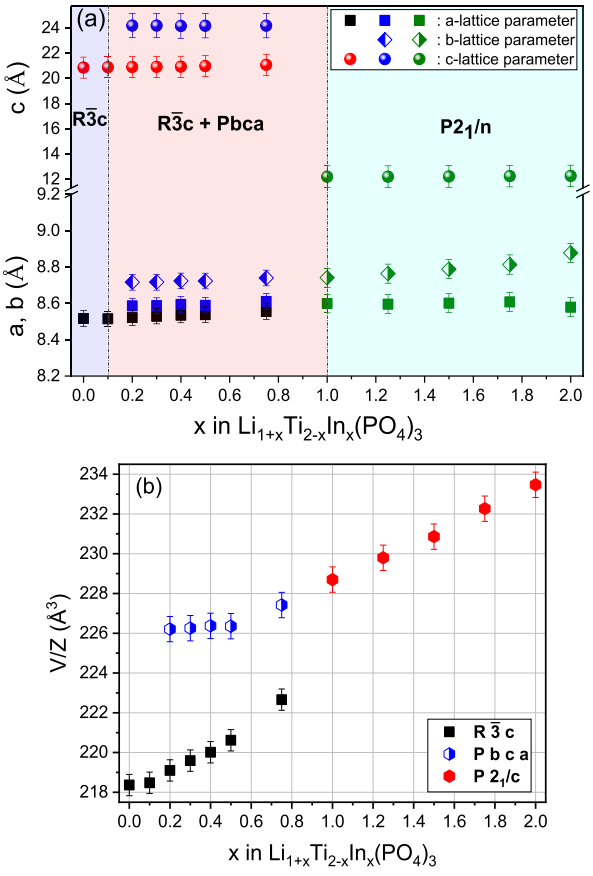

Figure 3. (a) Unit-cell parameters of three detected phases in the $Li_{1+x}Ti_{2-x}In_x(PO_4)_3$ $(0 \le x \le 2)$ samples. (b) Evolution of volume/structural formula (s.f.) in three analyzed phases.

The position of diffraction peaks shifts toward lower 2θ angles when x (In) content increases, indicating an increment of unit-cell parameters when Ti^{4+} (0.60 Å) is substituted by In^{3+} (0.80 Å) cations.[25] Unit-cell parameters and volume/structural formula (s.f.) are given in Figure 3a,b. The compositional dependence of the unit-cell volume increased with the In content; however, the volume was bigger in orthorhombic and monoclinic phases than in the rhombohe-

https://doi.org/10.1021/acs.inorgchem.4c00289
Inorg. Chem. 2024, 63, 7806−7819

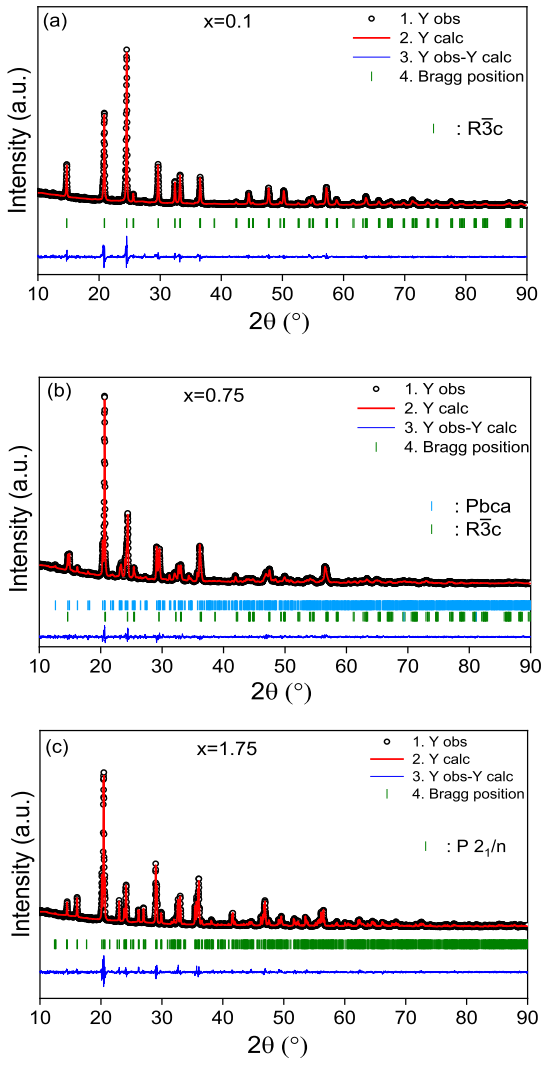

Figure 4. Rietveld refinement patterns recorded at room temperature on (a) x = 0.1, (b) x = 0.75, and (c) x = 1.75 samples given as the example. In these figures, the calculated and observed profiles are included. The difference between these profiles is shown underneath.

dral phase. To deduce relative amounts (%) of detected phases, the Rietveld fitting of XRD patterns was used.[28,29]

3.1.1. Structural Refinements. In the second stage, the structural refinement of phases was performed permitting a determination of structural site parameters (positions, thermal factors, and site occupancies). This analysis was performed with the FullProf program. Taking into account the big number of parameters, structural refinements were performed in separated steps; in the first one, the positions and occupancy of octahedral sites were deduced, assuming the nominal Ti^{4+} and In^{3+}composition of samples in starting models. In the second step, P and O atom parameters were refined; for that, thermal factors of Ti/In and P atoms were fixed at 0.5, O atoms at 1, and Li ions at 1.5 in the rhombohedral phase, while they were fixed at 0.85 for Ti/In and P atoms, 2.5 for O, and 2.5 for Li in orthorhombic and monoclinic phases. The fitting of experimental data was controlled through the "goodness of fit" χ^2 and R factors (R_{wp}: weighted-profile, R_b: Bragg factor, and R_p: profile factor). These parameters are given in Table S4, where the relative percentages of phases are included.

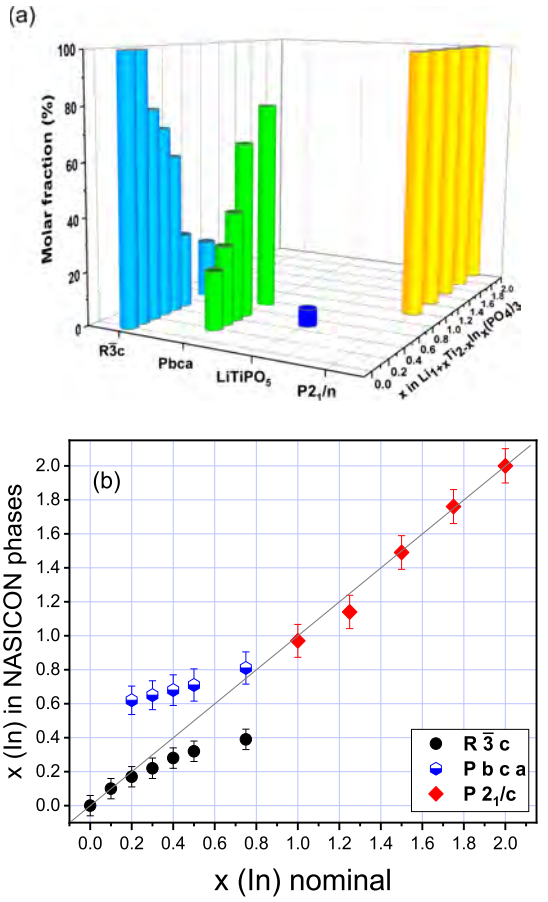

Figure 5. (a) Evolution of relative percentages of detected phases with x (In) content. (b) Evolution of x (In) content in three detected phases.

As illustrative examples, XRD patterns of x = 0.1, 0.75, and 1.75 samples, fitted with $R\bar{3}c$, *Pbca*, and $P2_1/n$ models, are given in Figure 4a–c. From Rietveld refinements, it was possible to deduce molar fractions (%) of different phases. Figure 5a shows the molar percentages of phases along the $Li_{1+x}Ti_{2-x}In_x(PO_4)_3$ ($0 \le x \le 2$) series. The samples x = 0 and x = 0.1, exhibited single rhombohedral phases; but in $0.2 \le x \le 0.75$ materials, the incorporation of In^{3+} favors the formation of orthorhombic phases. The molar fraction of orthorhombic phases increased from 21.8% for x = 0.2–78.1% for x = 0.75. In $1 \le x \le 2$ samples, monoclinic were detected as unique phases.

The resulting models confirmed the relative disposition of structural units in three phases (see Figure 1). In Tables S5–S7, P–O and Ti/In–O bonds and P–O–Ti/In angles, deduced in three phases, are reported. In general, it is observed that when x (In) increases, the mean Ti/In–O distances increase. When site occupancy is analyzed, it is observed that Ti^{4+} or In^{3+} cations do not display a clear preference for different octahedral sites.

In Figure 5b, it is observed that the amount of x (In) increases with the In composition of rhombohedral phases, achieving the limit $x \sim 0.4$ for the nominal x = 0.75 sample. The relative amount of rhombohedral phases increases when the temperature of preparation increased at 950 °C. At intermediate $0.2 \le x \le 0.75$ compositions, the x (In) content of orthorhombic phases increases slightly from 0.6 to 0.85/structural formula. Above x = 1, the orthorhombic phases were substituted by monoclinic ones, and the x (In) content

https://doi.org/10.1021/acs.inorgchem.4c00289
Inorg. Chem. 2024, 63, 7806–7819

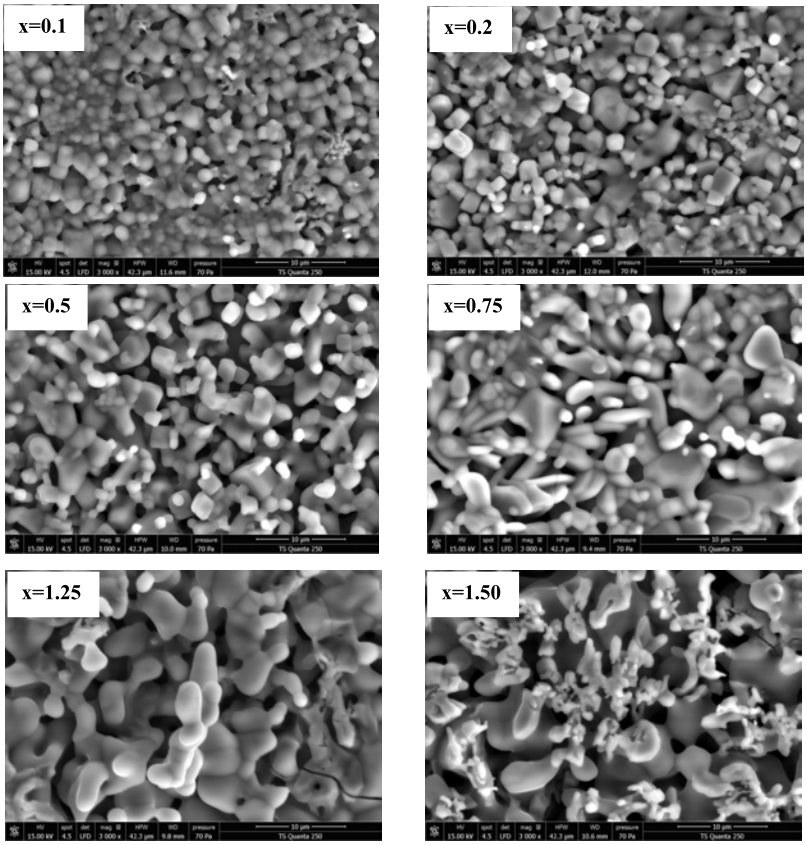

Figure 6. SEM images of $Li_{1+x}Ti_{2-x}In_x(PO_4)_3$ (x = 0.1; 0.2; 0.5; 0.75; 1.25, and 1.50) samples sintered at 950 °C.

increases in a linear way. From the relative percentages of phases and occupation of octahedral sites, the amount of indium was deduced in different phases (Figure 5b).

3.2. Sample Microstructure. SEM images of $Li_{1+x}Ti_{2-x}In_x(PO_4)_3$ samples are given in Figure 6. The analysis of micrographs shows the progressive increment of the pellet densification with In content. SEM micrographs show particles of different sizes and contrasts that were ascribed to different phases. In samples with $0 < x < 0.4$, the presence of small rounded/cubic particles, measuring less than 3 μm, have been associated with the rhombohedral phase. In the case of the sample x = 0.5, the crystallites exhibit a significant enlargement (~6 μm).

In orthorhombic samples, SEM images reveal the formation of elongated agglomerates of 8 μm length and 3 μm thickness. These agglomerates decrease in the compositional range $0.75 < x < 1.25$ samples. In monoclinic samples, the particle size decreased to 1 or 2 μm, and agglomerates change decreasing the thickness of particles while maintaining their elongated morphology.

Table S8 presents the relative density of $Li_{1+x}Ti_{2-x}In_x(PO_4)_3$ samples sintered at 950 °C for 8 h. The highest relative density was achieved in x = 0.2 (96%), surpassing that (75%) measured in the LTP sample. As the x(In) content increases ($x > 0.2$), the relative densities decrease, with a sharp decrement at x = 1 (76%) that was attributed to the orthorhombic → monoclinic transformation. In monoclinic phases ($1 \leq x \leq 2$), the relative density of pellets increased again, displaying a maximum at x = 1.25.

3.3. MAS NMR. MAS NMR spectroscopy was used to investigate the local structure and mobility of lithium in different phases. In some cases, the distribution of Ti^{4+} and In^{3+} cations around PO_4 tetrahedra was deduced by ^{31}P MAS NMR spectroscopy. In the case of lithium, the site occupancy and mobility were investigated with ^{6}Li and ^{7}Li MAS NMR techniques.

3.3.1. ^{31}P MAS NMR. In the $Li_{1+x}Ti_{2-x}In_x(PO_4)_3$ ($0 \leq x \leq 2$) series, the XRD patterns showed that rhombohedral phases are only present in the region $x \leq 0.2$, but rhombohedral and orthorhombic phases coexist in the $0.2 \leq x \leq 0.75$ range. In $1 \leq x \leq 2$ samples, only monoclinic phases were detected.

The ^{31}P MAS NMR spectra of the $Li_{1+x}Ti_{2-x}In_x(PO_4)_3$ ($0 \leq x \leq 2$) samples are given in Figure 7a. Taking into account that all detected phases display similar structural units, it was assumed that the chemical shift values of P atoms are similar in three phases. In the analyzed phases, five chemical environments (4Ti, 3Ti1In, 2Ti2In, 1Ti3In, and 4In) were considered around P tetrahedra, shifting the position of P components toward more positive values as the amount of indium increases[13,15] (Figure 3 and Table S4). This shift has permitted the simultaneous detection of NMR components of rhombohedral and orthorhombic/monoclinic phases.

On the other hand, XRD refinements showed that rhombohedral phases have one crystallographic P site, but orthorhombic and monoclinic phases display three sites. In the monoclinic x = 2 phase, where all P atoms are surrounded by 4In atoms, the ^{31}P MAS NMR spectrum displays the presence of three components at −5.02, −6.05, and −1.02 ppm of equal intensity. The existence of three P sites requires the presence of 15 ^{31}P NMR components; however, the resolution of 10 components suggests the presence of two similar tetrahedra in orthorhombic and monoclinic phases. At intermediate

https://doi.org/10.1021/acs.inorgchem.4c00289
Inorg. Chem. 2024, 63, 7806−7819

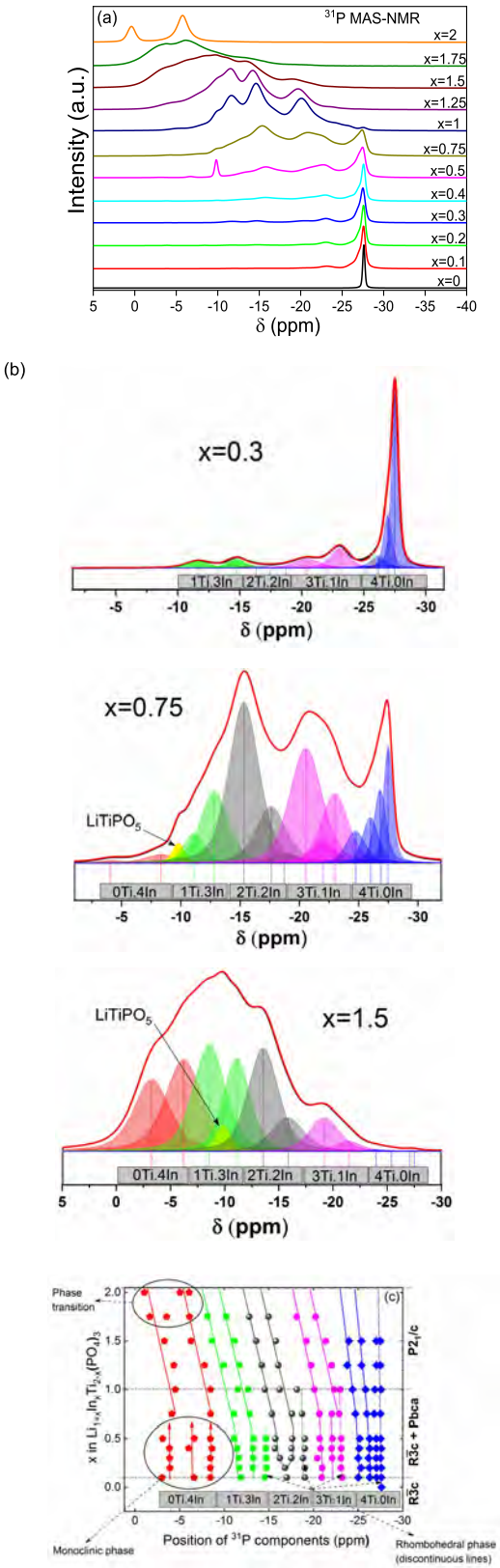

Figure 7. (a) ^{31}P MAS NMR spectra of $Li_{1+x}Ti_{2-x}In_x(PO_4)_3$ ($0 \le x \le 2$) samples. (b) Deconvolution of $x = 0.3$, $x = 0.75$, and $x = 1.5$ spectra given as examples. Positions of 4Ti, 3Ti1In, 2Ti2In, 1Ti3In, and 4In values are indicated. (c) Variation of chemical shift values of components with the composition of $Li_{1+x}Ti_{2-x}In_x$ $(PO_4)_3$ ($0 \le x \le 2$) samples.

compositions ($0.3 \le x \le 1.5$ samples), an additional component at −10 ppm was associated with the $LiTiPO_5$ phase, increasing slightly in samples prepared at 950 °C.

The deconvolution of ^{31}P MAS NMR spectra of $Li_{1.3}Ti_{1.7}In_{0.3}(PO_4)_3$ ($x = 0.3$), $Li_{1.75}Ti_{1.25}In_{0.75}(PO_4)_3$ ($x = 0.75$), and $Li_{2.5}Ti_{0.5}In_{1.5}(PO_4)_3$ ($x = 1.5$) phases are given as examples of formed phases, Figure 7b. According to above ideas, $Ti_{2-n}In_n$ environments were ascribed to each component in rhombohedral, but two components were required in orthorhombic or monoclinic phases (same color, Figure 7c). The result of the ^{31}P MAS NMR spectra deconvolution is given in Tables 1 and 2.

In $0 \le x \le 0.75$ samples, rhombohedral and orthorhombic patterns were detected in ^{31}P MAS NMR spectra. According to the phase composition, three $P(OTi)_{4-n}In_n$ environments ($x = 0$, 1, and 2) were detected in rhombohedral phases but five ($n = 0$, 1, 2, 3, and 4) in orthorhombic and monoclinic phases (see Figure 7b,c). From the relative intensity of $Ti_{4-n}In_n$ components, the compositional ratio In^{3+}/Ti^{4+} was deduced with the expression

$$\frac{In^{3+}}{Ti^{4+}} = \frac{1I_1 + 2I_2 + 3I_3 + 4I_4}{4I_0 + 3I_1 + 2I_2 + 1I_3} = \frac{x}{2 - x} \quad (1)$$

where Ti^{4+} and In^{3+} stand for the intensity of $Ti_{4-n}In_n$ NMR components (see Table 2). From the In^{3+}/Ti^{4+} ratios, the octahedral $Ti_{2-n}In_n$ composition of phases can also be estimated.

From the addition of $Ti_{2-n}In_n$ bands of three phases, the mean composition of samples was first deduced. The compositions deduced by NMR agree reasonably well with the nominal compositions, validating the assignment of components (Table 3 and Figure 7). The resolution of two $Ti_{2-n}In_n$ different sets allowed a determination of chemical composition of rhombohedral and orthorhombic phases. This analysis confirmed that the x (In) content of rhombohedral samples remained below 0.4/structural formula and displayed a small increment between 0.7 and 0.9 in orthorhombic phases. In $x > 1$ samples, the symmetry becomes monoclinic, and x (In) content increased linearly with composition.

3.3.2. ^{6}Li MAS NMR. As a consequence of smaller dipolar and quadrupolar interactions, ^{6}Li NMR components are narrowed with respect to those of ^{7}Li NMR ones (Figures 8, 9, and Table 4). This attenuation is responsible for the increment of resolution observed in ^{6}Li MAS NMR spectra. According to the XRD analysis, the ^{6}Li signal at ∼−1.1 ppm was ascribed to rhombohedral phases, while that at ∼−0.6 ppm was attributed to orthorhombic phases. In monoclinic phases, the position of the Li signal is near that detected in orthorhombic phases, indicating that the two structures are related.

Li ions with restricted mobility display broader NMR components than mobile Li ions. In Li poor rhombohedral phases ($x < 0.2$), the mobility of lithium is limited, making that central components be broadened by site heterogeneity. When the Li content increases, Li1−Li3 exchanges, decreasing the line-width of components with mobility. The formation of orthorhombic phases is responsible for the detection of two components. The absence of lithium exchanges between Li ions of rhombohedral and orthorhombic phases made possible to estimate relative amounts of lithium in two phases in the $0.2 < x < 0.75$ interval (Table S4). The analysis of this table showed that relative amounts of detected phases agree

https://doi.org/10.1021/acs.inorgchem.4c00289
Inorg. Chem. 2024, 63, 7806−7819

Table 1. Position (ppm) of ^{31}P MAS NMR Components of $Li_{1+x}Ti_{2-x}In_x(PO_4)_3$ ($0 \le x \le 2$) Samples[a]

envir.	$In_{0.1}P$	$In_{0.2}P$	$In_{0.3}P$	$In_{0.3}P$ (950 °C)	$In_{0.4}P$	$In_{0.4}P$ (950 °C)	$In_{0.5}P$	$In_{0.5}P$ (950 °C)	$In_{0.75}P$	$In_{1.0}P$	$In_{1.25}P$	$In_{1.5}P$	$In_{1.75}P$	$In_{2.0}P$
4Ti0In	−27.60	−27.60	−27.51	−27.51	−27.60	−27.51	−27.53	−27.53	−27.50	−27.56	−27.50	−27.50		
	−27.06	−27.05	−26.93	−27.02	−27.03	−27.02	−27.03	−27.02	−26.81	−26.87	−27.05	−27.04		
	−26.28	−26.25	−26.16	−26.04	−26.29	−25.93	−26.28	−25.99	−25.97	−25.84	−25.38	−25.38		
	−25.02	−25.32	−25.01	−25.02	−25.12	−24.89	−25.19	−25.01	−24.70	−24.37	−23.77	−23.96		
3Ti1In	−23.19	−23.07	−23.07	−23.18	−23.10	−23.18	−23.09	−23.18	−22.87	−22.98	−22.03	−21.37	−20.23	
			−22.09	−23.29	−22.03	−22.21	−22.12	−22.28	−22.04	−22.30				
	−20.90	−20.96	−20.41	−20.49	−20.79	−20.50	−20.68	−20.69	−20.65	−20.08	−19.72	−19.18	−18.12	
2Ti2In	−19.03	−19.01	−18.81	−18.32	−19.02	−18.31	−19.02	−18.63	−18.71	−18.13	−16.04	−15.77	−14.95	
			−17.50	−16.89	−17.53	−16.83	−17.61	−17.02	−17.58	−16.21				
	−16.99	−16.79	−16.21	−15.61	−15.66	−15.60	−15.72	−15.60	−15.33	−14.53	−14.19	−13.56	−12.79	
1Ti3In	−14.57	−14.75	−14.70	−14.71	−14.68	−14.53	−14.69	−14.52	−12.85	−12.69	−11.68	−11.12	−10.22	
		−13.21	−13.22	−13.37	−13.22	−13.21	−13.28	−13.22						
	−11.85	−11.67	−11.64	−11.03	−11.44	−11.19	−11.10	11.03	−11.09	−11.52	−9.98	−8.63	−8.13	
0Ti4In	−8.42	−8.42	−8.42	−8.46	−8.62		−8.44		−8.45	−8.45	−7.77	−6.24	−6.09	−5.02/ −6.05
	−3.01/ −6.60	−3.89	−3.87	−3.19/− 6.51	−3.84/ −6.01	−3.20/− 6.58	−3.09/ −6.62	−3.29/− 6.68	−4.10	−4.51	−4.33	−3.28	−1.65/ −3.52	−1.02
$LiTiPO_5$				−9.95	−9.92	−9.91	−9.83	−9.83	−9.79	−9.83	−9.89	−9.82		

[a]The results of some samples (x = 0.3, 0.4, and 0.5) prepared at 950 °C are also included.

reasonably well with those deduced by XRD and ^{31}P MAS NMR techniques.

In monoclinic phases, Li mobility is considerable, making that ^{6}Li NMR components should be narrowed; however, the increment of Li ions produces highly correlated motions that increase the line-width of components. The transformation of orthorhombic into monoclinic phases shows that the two detected components at ∼−1.3 and ∼−0.4 ppm correspond to Li species with different characteristics in monoclinic phases.

3.3.3. ^{7}Li MAS NMR. ^{7}Li MAS NMR spectra of the $Li_{1+x}Ti_{2-x}In_x(PO_4)_3$ ($0 \le x \le 2$) series are given in Figure 9. In general, ^{7}Li MAS NMR spectra are formed by central and spinning sidebands, that were used to deduce quadrupolar interactions. In rhombohedral phases, Li ions are located at triangular M12 windows, making that quadruple $\nu_Q$constants be near 24 kHz. When the Li content increases, mobility increases and line-width of components decrease.[11] The formation of orthorhombic phases shifts the central component toward more positive values, increasing the ν_Q constants to ∼60 kHz.

In monoclinic phases, Li mobility produces the cancelation of dipolar and quadruple interactions, resulting in narrowed MAS NMR patterns. When the central components are analyzed, two bands with different line-widths were detected that correspond to Li ions with different mobilities. In monoclinic samples, the detection of smaller quadrupolar interactions suggest the presence of reduced distortions in Li polyhedra. In Table 5, chemical shifts, quadrupolar constants, and intensity of components are depicted. The parameters deduced from ^{6}Li differ from those deduced for ^{7}Li NMR spectra, suggesting that values deduced in the last case are less reliable as a consequence of the lower resolution.

4. ELECTRICAL PROPERTIES

The Li conductivity of solid electrolytes changes with the structure and composition of phases. To evaluate the effect of the indium content on the transport properties of samples, IS was used.

Figure 10 displays the frequency dependence of the real part of Li conductivity of $Li_{1+x}Ti_{2-x}In_x(PO_4)_3$ ($0 \le x \le 2$) samples. To deduce "bulk" conductivity, the frequency range was extended from 10^2 Hz to 3×10^9 Hz. Impedance data of samples were normalized to the thickness and electrode area of pellets. From the analysis performed with complex nonlinear least-squares techniques, "bulk," "overall," and "electrode" contributions were deduced. The measured "bulk" and "overall" contributions result from the average of different particle shapes and compositions of different phases, showing that the measured values should be considered as apparent values. The equivalent circuit used for data analysis includes apparent R_b "bulk" and R_{gb} "grain boundary" resistances in parallel with the corresponding C_b and C_{gb} capacitances. In this analysis, the "overall" resistance $R_{ov} = R_b + R_{gb}$ and $\sigma_{ov} = 1/R_{ova}$. In equivalent circuits, a blocking "electrode" with a constant phase element was considered.

In $0 \le x \le 0.2$ samples, apparent "bulk" conductivity and activation energy of rhombohedral phases were deduced. However, apparent "bulk" contributions of rhombohedral and orthorhombic phases were hardly deduced in $0.2 \le x \le 1$ samples because of structural disorder. In monoclinic $1 \le x \le 2$ samples, the presence of two "bulk" contributions was ascribed to the presence of "core−shell" structures (green points of Figure 10).

The "overall" conductivity and activation energy of $Li_{1+x}Ti_{2-x}In_x(PO_4)_3$ ($0 \le x \le 2$) phases are given in Table 6. In Figure 11a, mean conductivity of $Li_{1+x}Ti_{2-x}In_x(PO_4)_3$ ($0 \le x \le 2$) samples was plotted versus reciprocal temperature ($1000/T$). Dc-conductivity values were fitted to the Arrhenius expression[13]

$$\sigma_{dc}T = A_0 \exp(-E_a/k_B T) \quad (2)$$

where σ_{dc}, k_B, T, A_0, and E_a are dc-conductivity, Boltzmann constant, absolute temperature (K), pre-exponential factor and activation energy, respectively.

The apparent "bulk" conductivity (σ_{bulk}) of rhombohedral phases increases from 7.6×10^{-6} S·cm^{-1} for x = 0, to 1.9×10^{-3} S·cm^{-1} for the x = 0.2 sample, displaying maximum conductivity and minimum activation energy of E_b = 0.27 eV (Figure 11a and Table 6). In x = 0.2 composition, the "overall" Li conductivity was $\sigma_{ov} = 1.7 \times 10^{-4}$ S·cm^{-1} and E_{ov} = 0.32 eV.

https://doi.org/10.1021/acs.inorgchem.4c00289
Inorg. Chem. 2024, 63, 7806−7819

Table 2. Relative Intensities (%) of ^{31}P MAS NMR Components in $Li_{1+x}Ti_{2-x}In_x(PO_4)_3$ ($0 \le x \le 2$) Series[a]

envir.	$In_{0,1}P$	$In_{0,2}P$	$In_{0,3}P$	$In_{0,3}P$ (950 °C)	$In_{0,4}P$	$In_{0,4}P$ (950 °C)	$In_{0,5}P$	$In_{0,5}P$ (950 °C)	$In_{0,75}P$	$In_{1,0}P$	$In_{1,25}P$	$In_{1,5}P$	$In_{1,75}P$	$In_{2,0}P$
4Ti0In	55.75	42.89	40.79	24.23	26.97	23.30	11.17	7.99	5.48	0.62	0.03	0.01		
	16.14	19.87	14.71	19.02	11.36	15.50	8.81	13.29	4.75	0.96	0.05	0.06		
	7.88	6.94	6.04	8.30	7.14	6.43	5.69	5.98	3.64	1.05	0.16	0.08		
	2.35	1.02	0.67	2.45	3.20	1.15	5.84	3.12	3.23	2.49	0.63	0.16		
3Ti1In	8.57	13.15	13.07	11.39	13.65	12.21	13.54	8.28	9.57	0.08			0.80	
			1.01	10.64	4.89	10.68	6.96	15.00	2.71	5.87	1.05	1.52	0.80	
	3.58	5.00	8.14	5.89	7.57	7.25	9.27	9.66	18.71	19.85	14.95	5.58	1.15	
2Ti2In	0.44	2.16	1.06	4.00	2.34	4.44	2.33	3.69	1.23	1.98				
	1.67	1.41	0.55	2.57	5.88	3.17	7.14	6.91	9.02	15.52	10.30	6.22	5.14	
			2.01	4.68	7.63	9.05	13.66	12.10	25.06	19.21	20.96	17.41	7.55	
1Ti3In	1.17	3.70	5.47	0.49	2.31	1.04	1.37	0.97						
		0.53	1.01	2.84	4.50	3.75	6.20	6.01	10.33	8.02	19.05	13.79	12.00	
	1.44	2.46	5.35	1.01	1.00	0.61	0.95	0.48	3.13	16.72	15.31	19.09	13.80	
0Ti4In	0.48	0.43	0.08	0.39	0.70		0.27		1.57	3.64	12.51	19.21	26.52	27.60/33.81
	0.29/0.24	0.44	0.05	0.19/0.34	0.13/0.16	0.06/0.15	0.33/0.63	0.11/0.50	0.35	0.90	4.64	14.78	10.58/22.50	38.59
$LiTiPO_5$				1.56	0.57	1.20	5.83	5.94	1.21	3.08	0.36	2.04		

[a]The results of some samples (x = 0.3, 0.4, and 0.5) prepared at 950 °C are also included.

Another maximum of conductivity was detected in the monoclinic $x \sim 1.25$ sample ($\sigma_{ov} = 1.4 \times 10^{-5}$ S·cm^{-1}), with an activation energy $E_{ov} = 0.39$ eV. The activation energy deduced for apparent "overall" and "bulk" contributions exhibits similar trends, albeit the apparent "bulk" values are consistently higher than the "overall" ones. The activation energies corresponding to the apparent "overall" conductivity and relative densities of $Li_{1+x}Ti_{2-x}In_x(PO_4)_3$ samples are depicted versus x (In) in Figure 11b.

5. DISCUSSION

The combined use of XRD, NMR, and IS techniques made possible the analysis of structural factors that enhance Li mobility in $Li_{1+x}Ti_{2-x}In_x(PO_4)_3$ samples. A first analysis was centered on the location of lithium ions in different phases. The increment of the Li content enhances Li−Li repulsions, destabilizing the Li coordination at structural sites. The relative importance of Li−O bonds and Li−Li repulsions define Li dynamics in analyzed samples.

5.1. Structural Characterization. *5.1.1. Crystalline Phases.* The linear increment of the unit-cell volume along the $Li_{1+x}Ti_{2-x}In_x(PO_4)_3$ series (Vegard's law) is justified by the substitution of Ti^{4+} (0.60 Å) by bigger In^{3+} (0.80 Å) cations (Figure 3a,b).[25] However, XRD patterns of $Li_{1+x}Ti_{2-x}In_x(PO_4)_3$ ($0 \le x \le 2$) samples showed the presence of three phases: (1) in the compositional range $0 \le x \le 0.2$, rhombohedral $R\bar{3}c$ phases are preponderant; (2) in the range $0 \le x \le 0.75$, the orthorhombic $Pbca$ phase increases at the expense of the rhombohedral one; (3) in the $1 \le x \le 2$ range, rhombohedral and orthorhombic phases disappeared and monoclinic $P2_1/n$ phases become dominant.

The absence of relevant amounts of secondary $InPO_4$ phases allowed the analysis of the sample composition and the distribution of In^{3+} ions in three phases.[13−15] All ^{31}P MAS NMR spectra display five components that were ascribed to P atoms surrounded by 4Ti, 3Ti1In, 2Ti2In, 1Ti3In, and 4In environments. The chemical shift values of different environments changes slightly with the sample composition, making still possible to define separated intervals for different environments. From the sum of relative intensities of five $Ti_{2-n}In_n$ environments, Ti^{4+}/In^{3+} ratios and averaged compositions of samples were estimated. The result of this analysis agrees well with the XRD results and nominal compositions of samples (Table 3). At intermediate compositions $0.4 < x < 0.75$, a small amount of the secondary $LiTiPO_5$ phase (narrow P component at ∼−10 ppm) was detected that did not affect considerably compositional determinations.

When the x (In) content increases, the positions of P components shift toward more positive values, making it possible to simultaneously detect different components for rhombohedral and orthorhombic/monoclinic phases. When $Ti_{2-n}In_n$ components of phases were considered in a separate way, the chemical compositions of rhombohedral and orthorhombic phases were deduced. In this analysis, it was confirmed that the x (In) content of orthorhombic phases is always higher than that of the rhombohedral phases (Table 3). The incorporation of x (In) content above 0.3/s.f. was not possible in rhombohedral phases, requiring the formation of orthorhombic phases with higher x (In) content (0.7−0.9/s.f.) to explain the average composition of samples. Above $x = 1$, the rhombohedral and orthorhombic phases disappear, and the x (In) content of monoclinic phases increases in a linear way

https://doi.org/10.1021/acs.inorgchem.4c00289
Inorg. Chem. 2024, 63, 7806−7819

Table 3. Nominal and Estimated x (In) Contents Deduced from Rietveld and ^{31}P MAS NMR Components in $Li_{1+x}Ti_{2-x}In_x(PO_4)_3$ ($0 \le x \le 2$) Samples

In_x	x = 0.1	x = 0.2	x = 0.3	x = 0.4	x = 0.5	x = 0.75	x = 1.0	x = 1.25	x = 1.5	x = 1.75	x = 2.0
$In_x^{Rietveld}$	0.10	0.25	0.34	0.44	0.56	0.72	0.97	1.14	1.49	1.75	2.0
$In_x^{NMR(31P)}$	0.12	0.22	0.29	0.42	0.56	0.75	0.98	1.10	1.48	1.75	2.0

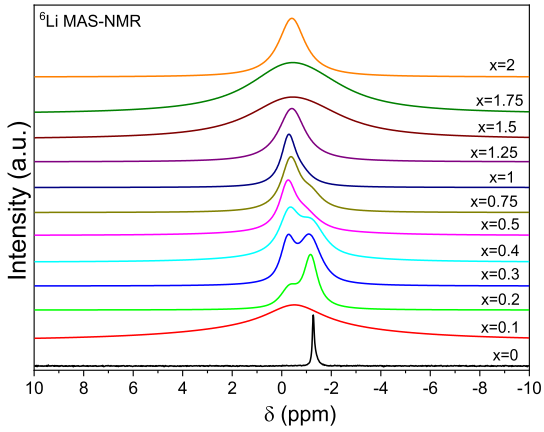

Figure 8. ^{6}Li MAS NMR spectra of $Li_{1+x}Ti_{2-x}In_x(PO_4)_3$ ($0 \le x \le 2$) samples.

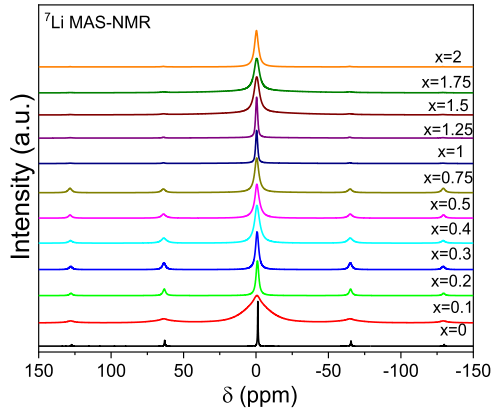

Figure 9. ^{7}Li MAS NMR spectra of $Li_{1+x}Ti_{2-x}In_x(PO_4)_3$ ($0 \le x \le 2$) samples.

with the sample composition. These results confirm basically the conclusions deduced from XRD analyses (Table 3).

5.1.2. Ti/In Distribution. In all samples, each P tetrahedron shares oxygens with four octahedra to form $M_2(PO_4)_3$ units. The rhombohedral phases display one P site, but orthorhombic and monoclinic phases display three P sites. Based on this fact, ^{31}P MAS NMR spectra should be formed by 5 components in rhombohedral (one site) but 15 components in orthorhombic or monoclinic phases (three sites). In the last two phases, however, only two tetrahedra are differentiated, making that the number of signals be reduced to 10. The orthorhombic and monoclinic phases display similar ^{31}P NMR shifts, suggesting that both phases are structurally related.

The composition of rhombohedral and orthorhombic phases was estimated from $Ti_{2-n}In_n$ components detected in ^{31}P NMR signal, giving values that agree with those deduced from nominal and structural analyses. In the orthorhombic and monoclinic phases, distribution of Ti^{4+} and In^{3+} cations was analyzed around two different tetrahedral sites. If In^{3+} cations were homogeneously dispersed, chemical compositions around two tetrahedral sites should be similar; however, octahedral compositions deduced were different, suggesting that distributions of Ti^{4+} and In^{3+} with respect two tetrahedra are slightly different.

If Ti^{4+} and In^{3+} cations are randomly distributed in a particular phase, the intensity of $Ti_{2-n}In_n$ components should agree with probabilities deduced from the binomial distribution

$$(a + b)^4 = a^4 + 4a^3b + 6a^2b^2 + 4ab^3 + b^4 \quad (3)$$

where a (Ti^{4+}) and b (In^{3+}) stand for relative occupations of octahedral sites. In random distributions, $4I_0/I_1$, $6I_1/4I_2$, $4I_2/6I_3$, and $I_3/4I_4$ ratios deduced from adjacent NMR components should agree with nominal a/b values. Deduced values were not the same, confirming deviations from the random distribution of Ti^{4+} and In^{3+} cations. Unfortunately, this analysis was not possible to be performed properly due to uncertainties associated with spectra deconvolution.

In structural analyses, the main conclusion referred to small variations on the x (In) content of rhombohedral ($0 < x < 0.3$) and orthorhombic ($x \sim 0.8$) phases. In monoclinic $x > 1$ phases, the x (In) contents increase in a linear way with nominal compositions (slope 1:1), suggesting a disordered distribution of Ti^{4+} and In^{3+} cations, compatible with the Vegard's law.

5.2. Li Conductivity. *5.2.1. Bulk Conductivity.* The substitution of Ti^{4+} by In^{3+} cations increases the amount of Li^+/structural formula, which reduces Li−Li distances and increases electrostatic repulsions. If vacant sites are near occupied sites, Li^+ions are forced to occupy more separated positions. To better understand transport properties, the occupation of Li sites along conduction channels has to be investigated. The number of sites occupied by lithium is two in rhombohedral and orthorhombic but three in monoclinic phases.

Figure 12 shows the arrangement of conduction channels deduced for two hoping distances (~4 and 6.8 Å) in three analyzed phases. In general, short Li−Li distances (3.3−3.6 Å) increase Li−Li repulsions making that Li separation increases and Li motions becomes more correlated. On the contrary, the increment of cation vacancies decreases the correlation degree.

In rhombohedral samples, 6-fold M1 sites are occupied in the starting member of the $Li_{1+x}Ti_{2-x}In_x(PO_4)_3$ series. In this composition, Li1−Li1 distances are ~6 Å and Li conductivity is $\sim 1 \times 10^{-5}$ S·cm^{-1}. In Li-richer samples, additional Li is accommodated at M3 sites, increasing considerably electrostatic Li1−Li3 repulsions ($d_{Li-Li} \sim 3.5$ Å). As a consequence of this interaction, cation vacancies are allocated at M1 sites and Li ions at M3 sites, increasing Li3−Li3 distances to ~6 Å.[32] The Li vacant sites produced at the intersection of three conduction channels enhances Li mobility along conduction channels, producing a maximum of conductivity $\sim 1 \times 10^{-3}$ S·cm^{-1} in x = 0.2 composition. In rhombohedral samples, the Li^+ hopping is produced between Li1 and Li3 positions, making Li1−Li3−Li1−Li3 the most probable channels for conductivity. Above x = 0.2, Li motions become more correlated,

https://doi.org/10.1021/acs.inorgchem.4c00289
Inorg. Chem. 2024, 63, 7806−7819

Table 4. Chemical Shifts (ppm), Line-Width (ppm), and Relative Intensity (%) of ^{6}Li MAS NMR Components of $Li_{1+x}Ti_{2-x}In_x(PO_4)_3$ ($0 \le x \le 2$) Samples

In_x	x = 0.1	x = 0.2	x = 0.3	x = 0.4	x = 0.5	x = 0.75	x = 1.25	x = 1.5	x = 1.75	x = 2.0
rhombohedral										
δ_1	−0.4	−1.2	−1.1	−1.2	−1.0	−1.2				
$\Delta\nu$	9.5	0.7	1.1	1.2	1.3	1.1				
G/L	0	0	0	0	0	0				
I1 (%)	66	71	67	35	27	26				
orthorhombic										
δ_2	−0.5	−0.3	−0.2	−0.3	−0.2	−0.4				
$\Delta\nu$	2.8	0.9	0.7	1.0	0.8	0.9				
G/L	0	0	0	0	0	0				
I2 (%)	34	29	33	65	73	74				
monoclinic										
δ_3								−1.3	−1.3	−0.7
$\Delta\nu$								4	4	0.6
G/L								0	0	0
I3 (%)								31	37	69
δ_4							−0.4	−0.2	−0.2	−0.1
$\Delta\nu$							1.3	3.9	3.8	0.6
G/L							0	0	0	0
I4 (%)							100	69	63	31

Table 5. Chemical Shifts (ppm), Line-Width (ppm), and Relative Intensity (%) of ^{7}Li MAS NMR Components of $Li_{1+x}Ti_{2-x}In_x(PO_4)_3$ ($0 \le x \le 2$) Samples[a]

In_x	x = 0.1	x = 0.2	x = 0.3	x = 0.4	x = 0.5	x = 0.75	x = 1.25	x = 1.5	x = 1.75	x = 2.0
rhombohedral										
δ_1	**−0.6**	**−1.0**	**−0.9**	**−0.8**	**−0.8**	**−0.6**				
$\Delta\nu$	2.2	2.2	2.6	5.0	5.0	4.0				
G/L	0	0	0	0	0	0				
ν_Q	**17**	**24**	**24**	**18**	**17**	**13**				
η	0	0	0	0	0	0				
I1 (%)	**85**	**87**	**70**	**78**	**60**	**33**				
orthorhombic										
δ_2	**−0.6**	**−0.5**	**−0.5**	**−0.5**	**−0.5**	**−0.4**				
$\Delta\nu$	5.0	2.2	2.4	2.4	2.4	3.0				
G/L	0	0	0	0	0	0				
ν_Q	**45**	**60**	**60**	**60**	**58**	**58**				
η	0	0	0	0	0	0				
I2 (%)	**15**	**13**	**30**	**22**	**40**	**67**				
monoclinic										
δ_3							**−2.3**	**−2.3**	**−2.2**	**−2.3**
$\Delta\nu$							2	4	4	70
G/L							0	0	0	
I3 (%)							**38**	**49**	**46**	**45**
δ_4							**−0.4**	**−0.4**	**−0.5**	**−0.4**
$\Delta\nu$							4	4.4	4.6	3
G/L							0	0	0	
ν_Q							**6**	**6**	**6**	**6**
η							0	0	0	
I4 (%)							**62**	**51**	**54**	**55**

[a]Quadruple parameters ν_Q(kHz) and η (dimensionless) have been included.

decreasing the conductivity and increasing the activation energy.

In orthorhombic samples, 6- and 8-fold coordination of Li^+ ions is produced at two tetrahedral sites: Li1 sites (Li1−O distance ∼2.01 Å) and Li2 sites where Li ions display bigger mobility (Li2−O distance ∼2.30 Å) (Table S6). In orthorhombic samples, there are two Li sites involved in monodimensional motions along a and b axes in two different planes. In the first case, Li1−Li1 distances are near 4.7 Å and distances between contiguous zigzag chains are ∼5.7 Å. In the second case, Li2−Li2 distances are near 4.6 Å and distance between chains are 3.1 Å, making more favorable bidimensional motions in one of ab-planes.

In the $0.2 \le x \le 0.75$ interval, one "plateau" of conductivity was related to the rhombohedral phase (near 10^8 Hz) and another narrow one (at 10^6 Hz) to orthorhombic phases (red

https://doi.org/10.1021/acs.inorgchem.4c00289
Inorg. Chem. 2024, 63, 7806−7819

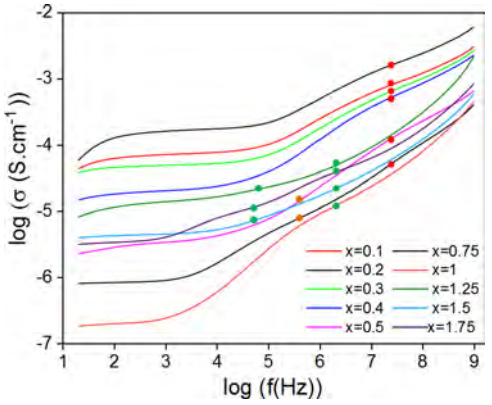

Figure 10. Frequency dependence of real conductivity of $Li_{1+x}Ti_{2-x}In_x(PO_4)_3$ ($0 \le x \le 2$) samples.

and orange points of Figure 10). For the $x = 0.2$ composition, apparent "bulk" conductivity displays a maximum, despite the presence of 20% of the orthorhombic phase. Small changes were detected in $x = 0.3$ and $x = 0.4$ samples, where the volume fraction of orthorhombic phase increases from 30 to 40% (Table S4). The molar fraction of orthorhombic phases increases up to 60 and 70% in $x = 0.5$ and 0.75 samples. From these results, it is possible to state that the increment of the volume fraction of the less conductive orthorhombic phase reduces the mean apparent "bulk" conductivity of samples.

In monoclinic samples, there are three crystallographic positions. The Li1 cation forms a regular tetrahedral coordination with oxygen atoms, while the Li2 and Li3 cations adopt a distorted trigonal bipyramidal coordination. In these samples Li2−Li3 distances are 3.0 and 3.3 Å, favoring Li motions along monodimensional chains disposed parallel to the *b* axis. The parallel chains are connected through Li2−Li2 pairs, separated 3.9 Å along the *c*-axis. From this fact, bidimensional motions are easily produced in monoclinic phases. The increment of temperature should favor an increment on the channels dimensionality. In monoclinic samples, Li conductivity displays a maximum at $x = 1.25$/structural formula, decreasing again when x (In) increases, and Li motions become more correlated.

For higher x (In) increments ($x > 1$), the admittance curve of monoclinic phases changes to a single plateau at frequencies close to 10^7 Hz. The definition of the apparent "bulk" plateau

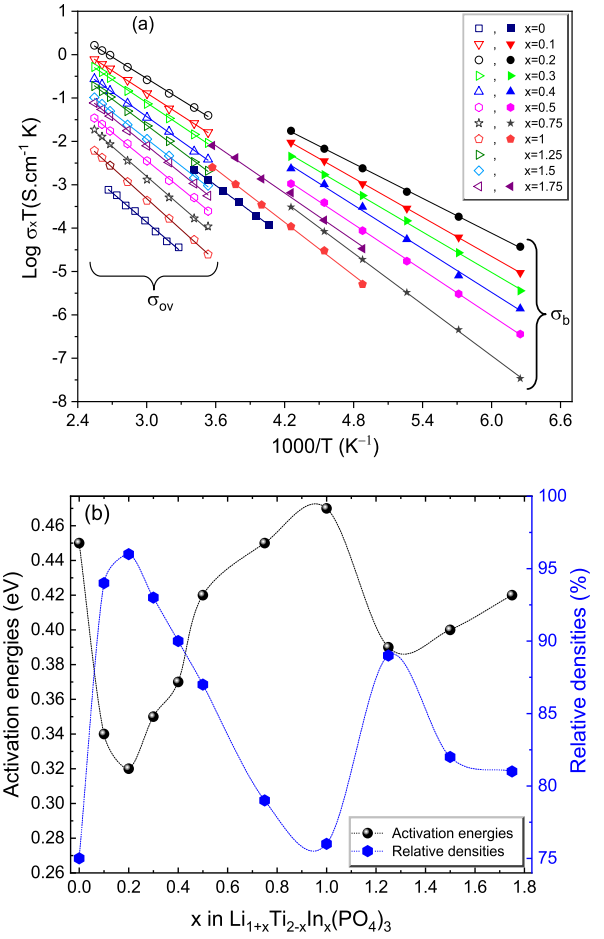

Figure 11. (a) Arrhenius plots of "bulk" (closed symbols) and "overall" (open symbols) dc conductivities of $Li_{1+x}Ti_{2-x}In_x(PO_4)_3$ ($0 \le x \le 2$) samples (b) activation energies corresponding to apparent "overall" conductivity (black symbols) and relative densities (blue symbols) as a function of composition x in $Li_{1+x}Ti_{2-x}In_x(PO_4)_3$. The dotted lines are drawn to guide the eye. The sample with $x = 0.2$ shows the highest relative density with the minimum of activation energy.

becomes difficult as a consequence of compositional heterogeneities. At $x = 1.25$, 1.5, and 1.75 samples, two apparent "bulk" plateaus were detected that correspond to

Table 6. Apparent "Bulk" and "Overall" Conductivity of $Li_{1+x}Ti_{2-x}In_x(PO_4)_3$ ($0 \le x \le 2$) Samples Measured at Room Temperature[a]

	"bulk" conductivity			"overall" conductivity		
In_x	σ (S·cm^{-1})	A_0 (S·cm^{-1})	E_a (eV)	σ (S·cm^{-1})	A_0 (S·cm^{-1})	E_a (eV)
0.0	7.61×10^{-6}	3.01×10^{4}	0.39	1.18×10^{-7}	1.10×10^{4}	0.45
0.1	9.52×10^{-4}	2.34×10^{4}	0.30	7.36×10^{-5}	1.80×10^{4}	0.34
0.2	1.90×10^{-3}	8.31×10^{3}	0.27	1.70×10^{-4}	2.40×10^{4}	0.32
0.3	8.21×10^{-4}	1.99×10^{4}	0.31	4.92×10^{-5}	1.66×10^{4}	0.35
0.4	6.48×10^{-4}	3.71×10^{4}	0.33	1.99×10^{-5}	1.62×10^{4}	0.37
0.5	2.74×10^{-4}	3.23×10^{4}	0.35	3.15×10^{-6}	1.07×10^{4}	0.42
0.75	5.32×10^{-5}	7.58×10^{4}	0.39	8.32×10^{-7}	1.20×10^{4}	0.45
1	3.73×10^{-5}	5.12×10^{4}	0.40	2.01×10^{-7}	7.08×10^{3}	0.47
1.25	2.58×10^{-4}			1.37×10^{-5}		0.39
1.5	5.19×10^{-5}			4.37×10^{-6}		0.40
1.75	6.33×10^{-5}	2.88×10^{4}	0.37	3.34×10^{-6}	2.09×10^{4}	0.42

[a]Activation energy (E_a) and pre-exponential factor (A_0) deduced from Arrhenius plots.

https://doi.org/10.1021/acs.inorgchem.4c00289
Inorg. Chem. 2024, 63, 7806−7819

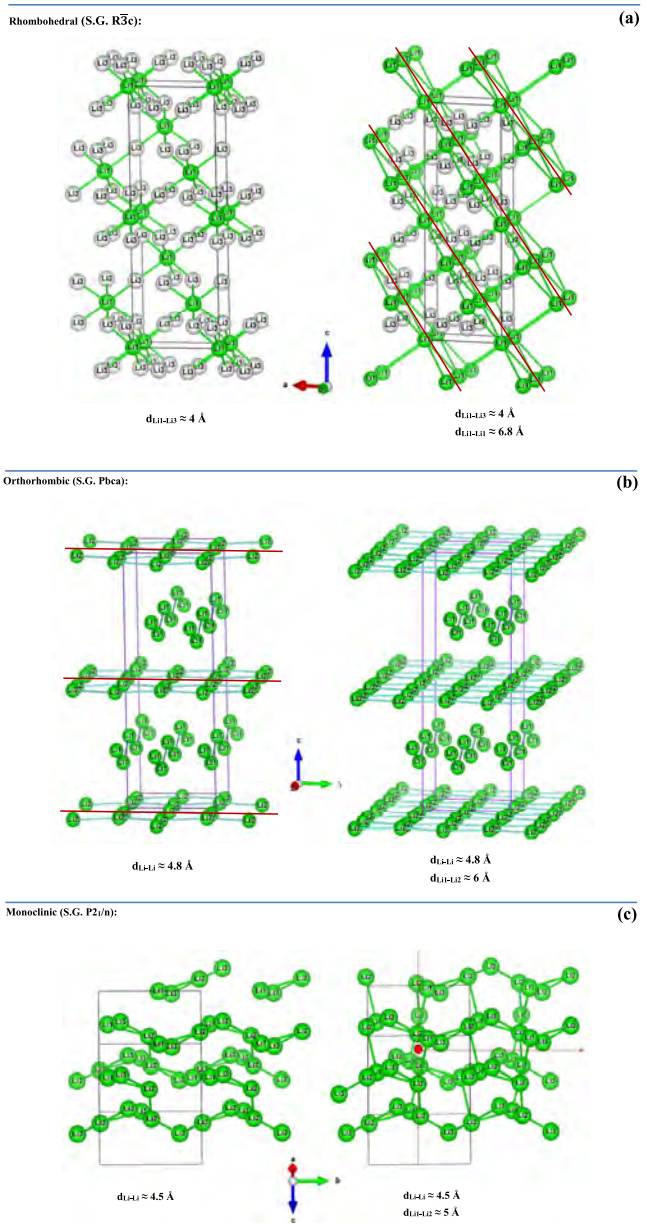

Figure 12. Schematic representation of conduction channels in three detected $Li_{1+x}Ti_{2-x}In_x(PO_4)_3$ phases; (a) rhombohedral (S.G. $R\bar{3}c$), (b) orthorhombic (S.G. *Pbca*), and (c) monoclinic (S.G. $P2_1/n$).

core−shell structures, where shells display lower ionic conductivity than cores.[13,33] The absence of orthorhombic phases improves densification, detecting a maximum of apparent "bulk" conductivity at $x \sim 1.25$/structural formula.

If it is assumed that the activation energy required for Li hopping between equivalent sites increases with distance, we can conclude that in rhombohedral samples, correlated three-dimensional Li motions are caused by the Li hopping between sites separated by 3.6 Å. In the case of monoclinic samples, bidimensional motions are produced in bc-planes by hopping of lithium between sites separated by 3 and 3.3 Å. In the case of orthorhombic samples, monodimensional motions are produced by Li hopping between sites separated by ∼4.6 Å along *a* and *b* directions. This observation explains the conductivity values detected in three analyzed phases.

5.2.2. Grain-Boundary Conductivity. Activation energies corresponding to apparent "overall" conductivity and relative densities of $Li_{1+x}Ti_{2-x}In_x(PO_4)_3$ samples are plotted vs x (In) in Figure 11b. From this plot, it can be concluded that the increment of density increases the "grain-boundary" conductivity, improving the "overall" conductivity of samples. A reduction of the sample porosity should increase the density of pellets. From the above considerations, it is clear that apparent "bulk" and "grain-boundary" conductivities display different optimization processes.

A steep decrease in activation energies, from 0.45 to 0.32 eV, is observed with increasing the relative densities of samples from 75 and 96% for x (In) going from $x = 0$ to $x = 0.2$. Above $x = 0.2$, the activation energies increase and the densities of the samples decrease until $x = 1$. Above $x = 1$, the opposite was observed for increasing x (In) contents. From Figure 11b, two maxima were detected being better that of rhombohedra samples.

The rhombohedral phases display a maximum in apparent "bulk" and "overall" conductivities at $x = 0.2$. The conductivity plot shifted to higher frequency, supporting a faster lithium dynamics at increasing x (In) contents. In monoclinic samples, maximum conductivity was detected at $x = 1.25$. In the case of orthorhombic samples, Li dynamics is poorer than in other two phases. A deeper study of structural changes produced along the series will permit in future works the optimization of transport properties.

6. CONCLUSIONS

The preparation of $Li_{1+x}Ti_{2-x}In_x(PO_4)_3$ ($0 \le x \le 2$) samples has permitted a better understanding of structure and Li mobility in rhombohedral, orthorhombic, and monoclinic phases. The deconvolution of ^{31}P MAS NMR spectra allowed the identification of 4Ti, 3Ti1In, 2Ti2In, 1Ti3In, and 4In bands in three phases and an estimation of the phase composition.

The dispersion of charge deficits (In atoms) favors long-range motions of Li^+ ions along conduction channels. In rhombohedral phases, electrostatic Li−Li repulsions favored the onset of more extended Li motions and a maximum of conductivity at $x \sim 0.2$/s.f. The increment of In^{3+} cations promotes the formation of orthorhombic and monoclinic phases, where structural units and conduction channels changed, decreasing Li mobility. The transformation of orthorhombic into monoclinic phases increased Li conductivity again, achieving a maximum at $x = 1.25$ composition.

The formation of less conducting orthorhombic phases reduced considerably the conductivity of samples in the compositional range $0.3 \le x \le 0.75$ samples as a consequence of the composite effect.

■ ASSOCIATED CONTENT

Supporting Information

The Supporting Information is available free of charge at https://pubs.acs.org/doi/10.1021/acs.inorgchem.4c00289.

Crystallographic data, selected bond distances and angles, and results from density measurements for $Li_{1+x}Ti_{2-x}In_x(PO_4)_3$ ($0 \le x \le 2$) samples (PDF)

■ AUTHOR INFORMATION

Corresponding Author

Radhouene Kahlaoui − *LR05ES09 Laboratoire d'Application de la Chimie aux Ressources et Substances Naturelles et à l'Environnement (LACReSNE), Université de Carthage,*

https://doi.org/10.1021/acs.inorgchem.4c00289
Inorg. Chem. 2024, 63, 7806−7819

Faculté des Sciences de Bizerte, Bizerte 7021, Tunisia; Instituto de Ciencia de Materiales de Madrid (ICMM), Consejo Superior de Investigaciónes Científicas (CSIC), Madrid 28049, Spain; orcid.org/0000-0002-7891-0691; Email: kradhouene960@gmail.com

Authors

Kamel Arbi − *Instituto de Ciencia de Materiales de Madrid (ICMM), Consejo Superior de Investigaciónes Científicas (CSIC), Madrid 28049, Spain*

Isabel Sobrados − *Instituto de Ciencia de Materiales de Madrid (ICMM), Consejo Superior de Investigaciónes Científicas (CSIC), Madrid 28049, Spain*

Ricardo Jimenez − *Instituto de Ciencia de Materiales de Madrid (ICMM), Consejo Superior de Investigaciónes Científicas (CSIC), Madrid 28049, Spain*

Riadh Ternane − *LR05ES09 Laboratoire d'Application de la Chimie aux Ressources et Substances Naturelles et à l'Environnement (LACReSNE), Université de Carthage, Faculté des Sciences de Bizerte, Bizerte 7021, Tunisia*

Jesus Sanz − *Instituto de Ciencia de Materiales de Madrid (ICMM), Consejo Superior de Investigaciónes Científicas (CSIC), Madrid 28049, Spain;* orcid.org/0000-0002-9179-2191

Complete contact information is available at: https://pubs.acs.org/10.1021/acs.inorgchem.4c00289

Notes

The authors declare no competing financial interest.

■ ACKNOWLEDGMENTS

The authors would like to thank the Spanish Ministry of Higher Education and Scientific Research for financial support. This research was funded by Spanish I-COOP 2021-COOPB20630 and MICIN agency (PID 2019-10666-2RB-042) projects.

■ REFERENCES

(1) Degen, F.; Winter, M.; Bendig, D.; Tübke, J. Energy consumption of current and future production of lithium-ion and post lithium-ion battery cells. *Nat. Energy* **2023**, *8*, 1284−1295.

(2) Zhu, J.; Zhao, J.; Xiang, Y.; Lin, M.; Wang, H.; Zheng, B.; He, H.; Wu, Q.; Huang, J. Y.; Yang, Y. Chemo-mechanical Failure Mechanism Study in NASICON-Type $Li_{1.3}Al_{0.3}Ti_{1.7}(PO_4)_3$ Solid-State Lithium Batteries. *Chem. Mater.* **2020**, *32*, 4998−5008.

(3) Goodenough, J. B.; Park, K. S. The Li-ion rechargeable battery: a perspective. *J. Am. Chem. Soc.* **2013**, *135*, 1167−1176.

(4) Winter, M.; Barnett, B.; Xu, K. Before Li Ion Batteries. *Chem. Rev.* **2018**, *118* (23), 11433−11456.

(5) Tong, D.; Zhang, Q.; Zheng, Y.; Caldeira, K.; Shearer, C.; Hong, C.; Qin, Y.; Davis, S. J. Committed emissions from existing energy infrastructure jeopardize 1.5 °C climate target. *Nat.* **2019**, *572* (7769), 373−377.

(6) Goodenough, J. B. Rechargeable batteries: challenges old and new. *J. Solid State Electrochem.* **2012**, *16*, 2019−2029.

(7) Xing, L.; Zheng, X.; Schroeder, M.; Alvarado, J.; Cresce, A. V. W.; Kang Xu, K.; Li, Q.; Li, W. Deciphering the Ethylene Carbonate−Propylene Carbonate Mystery in Li-Ion Batteries. *Acc. Chem. Res.* **2018**, *51* (2), 282−289.

(8) Bachman, J. C.; Muy, S.; Grimaud, A.; Chang, H. H.; Pour, N.; Lux, S. F.; Paschos, O.; Maglia, F.; Lupart, S.; Lamp, P.; Giordano, L.; Shao-Horn, Y. Inorganic Solid-State Electrolytes for Lithium Batteries: Mechanisms and Properties Governing Ion Conduction. *Chem. Rev.* **2016**, *116* (1), 140−162.

(9) Goodenough, J. B.; Hong, H. Y. P.; Kafalas, J. Fast Na^+-ion transport in skeleton structures. *Mater. Res. Bull.* **1976**, *11* (2), 203−220.

(10) Pinus, I. Y.; Shaikhlislamova, A. R.; Stenina, I. A.; Zhuravlev, N. A.; Yaroslavtsev, A. B. Phase Transitions of the NASICON-Type Mixed Phosphates $LiM_2(PO_4)_3$ (M = Ti, Zr) and $LiInNb(PO_4)_3$. *Inorg. Mater.* **2009**, *45* (12), 1370−1374.

(11) Arbi, K.; Hoelzel, M.; Kuhn, A.; García-Alvarado, F.; Sanz, J. Structural factors that enhance lithium mobility in fast-ion $Li_{1+x}Ti_{2-x}Al_x(PO_4)_3$ ($0 \le x \le 0.4$) conductors investigated by neutron diffraction in the temperature range 100−500 K. *Inorg. Chem.* **2013**, *52* (16), 9290−9296.

(12) Xu, T.; Zhao, M.; Su, Z.; Duan, W.; Shi, Y.; Li, Z.; Pol, V. G.; Song, X. Nanostructured $LiTi_2(PO_4)_3$ anode with superior lithium and sodium storage capability aqueous electrolytes. *J. Power Sources* **2021**, *481*, No. 229110.

(13) Kahlaoui, R.; Arbi, K.; Sobrados, I.; Jimenez, R.; Sanz, J.; Ternane, R. Cation miscibility and lithium mobility in NASICON $Li_{1+x}Ti_{2-x}Sc_x(PO_4)_3$ ($0 \le x \le 0.5$) series: a combined NMR and impedance study. *Inorg. Chem.* **2017**, *56* (3), 1216−1224.

(14) Aono, H.; Sugimoto, E.; Sadaoka, Y.; Imanoka, N.; Adachi, G. Ionic conductivity of solid electrolytes based on lithium titanium phosphate. *J. Electrochem. Soc.* **1990**, *137* (4), 1023−1027.

(15) Arbi, K.; Lazarraga, M. G.; Chehimi Ben Hassen, D.; Trabelsi, M. A.; Rojo, J. M.; Sanz, J. Lithium mobility in $Li_{1.2}Ti_{1.8}R_{0.2}(PO_4)_3$ compounds (R = Al, Ga, Sc, In) as followed by NMR and impedance spectroscopy. *Chem. Mater.* **2004**, *16* (2), 255−262.

(16) Perez-Estébanez, M.; Isasi-Marin, J.; Többens, D. M.; Rivera-Calzada, A.; León, C. A systematic study of Nasicon type $Li_{1+x}M_xTi_{2-x}(PO_4)_3$ (M: Cr, Al, Fe) by neutron diffraction and impedance spectroscopy. *Solid State Ion.* **2014**, *266*, 1−8.

(17) Catti, M.; Comotti, A.; Di Blas, S.; Ibberson, R. M. Extensive lithium disorder in $Li_{1.5}Fe_{0.5}Ti_{1.5}(PO_4)_3$ Nasicon by neutron diffraction, and the $Li_{1+x}Fe_xTi_{2-x}(PO_4)_3$ phase diagram. *J. Mater. Chem.* **2004**, *14* (5), 835−839.

(18) Monchak, M.; Hupfer, T.; Senyshyn, A.; Boysen, H.; Chernyshov, D.; Hansen, T.; Schell, K. G.; Bucharsky, E. C.; Hoffmann, M. J.; Ehrenberg, H. Lithium diffusion pathway in $Li_{(1.3)}Al_{(0.3)}Ti_{(1.7)}(PO_4)_3$ (LATP) superionic conductor. *Inorg. Chem.* **2016**, *55* (6), 2941−2945.

(19) Arbi, K.; Tabellout, M.; Sanz, J. NMR and electric impedance study of lithium mobility in fast ion conductors $LiTi_{2-x}Zr_x(PO_4)_3$ ($0 \le x \le 2$). *Solid State Ion.* **2010**, *180* (40), 1613−1619.

(20) Kahlaoui, R.; Arbi, K.; Jimenez, R.; Sobrados, I.; Sanz, J.; Ternane, R. Distribution and mobility of lithium in NASICON type $Li_{1-x}Ti_{2-x}Nb_x(PO_4)_3$ ($0 \le x \le 0.5$) compounds. *Mater. Res. Bull.* **2018**, *101*, 146−154.

(21) Morin, E.; Angenault, J.; Couturier, J. C.; Quarton, M.; He, H.; Klinowski, J. Phase transition and crystal structures of $LiSn_2(PO_4)_3$. *Eur. J. Solid State Inorg. Chem.* **1997**, *34* (9), 947−958.

(22) Catti, M.; Stramare, S.; Ibberson, R. Lithium location in NASICON-type Li^+ conductors by neutron diffraction. I. Triclinic α'-$LiZr_2(PO4)_3$. *Solid State Ion.* **1999**, *123*, 173−180.

(23) Losilla, E. R.; Aranda, M. A. G.; Martinez-Lara, M.; Bruque, S. Reversible triclinic-rhombohedral phase transition in $LiHf_2(PO_4)_3$: crystal structures from neutron powder diffraction. *Chem. Mater.* **1997**, *9* (7), 1678−1685.

(24) Weiss, M.; Weber, D. A.; Senyshyn, A.; Janek, J.; Zeier, W. G. Correlating transport and structural properties in $Li_{1+x}Al_xGe_{2-x}(PO_4)_3$ (LAGP) prepared from aqueous solution. *ACS Appl. Mater. Interfaces* **2018**, *10* (13), 10935−10944.

(25) Shannon, R. D. Revised effective ionic radii and systematic studies of interatomic distances in halides and chalcogenides. *Acta Crystallogr.* **1976**, *A32*, 751−767.

(26) Hamdoune, S.; Tran Qui, D.; Schouler, E. J. L. Ionic conductivity and crystal structure of $Li_{1+x}Ti_{2-x}In_x(PO_4)_3$. *Solid State Ion.* **1986**, *18*−*19*, 587−591.

(27) Qui, D. T.; Hamdoune, S.; Soubeyroux, J. L.; Prince, E. Neutron Powder Diffraction Study of Solid Solution $Li_{l+x}Ti_{2-x}In_x(PO_4)_3$. *J. Solid State Chem.* **1988**, *72* (2), 309−315.
(28) Rietveld, H. M. A Profile Refinement Method for Nuclear and Magnetic Structures. *J. Appl. Crystallogr.* **1969**, *2* (2), 65−71.
(29) Rodriguez-Carvajal, J. Recent Advances in Magnetic Structure Determination by Neutron Powder Diffraction. *Phys. B: Condens. Matter.* **1993**, *192* (1−2), 55−69.
(30) Bruker WINFIT program. *Bruker Rep.* **1994**, *140*, 43−46.
(31) Johnson, D., *Zview for Windows: A software Program for IES Analysis. Version 3.3a*; Scribner Associates Inc.: NC, USA, Inc., ©1990−2011.
(32) Zhang, X.; Butenko, D.; Gao, L.; Ye, X.; Hong, B.; Han, S.; Xia, W.; Wang, S.; Sun, Y.; Zhao, Y.; Zhu, J. Synergistic Ion Diffusion in Lithium Titanium Phosphate Conductors: A Tale from Solo to Ensemble. *Chem. Mater.* **2023**, *35* (11), 4541−4548.
(33) Arbi, K.; Bucheli, W.; Jimenez, R.; Sanz, J. High lithium ion conducting solid electrolytes based on NASICON $Li_{1+x}Al_xM_{2-x}(PO_4)_3$ materials (M = Ti, Ge and $0 \leq x \leq 0.5$). *J. Eur. Ceram. Soc.* **2015**, *35* (5), 1477−1484.

https://doi.org/10.1021/acs.inorgchem.4c00289
Inorg. Chem. 2024, 63, 7806−7819